

The International Journal of Robotics Research

<http://ijr.sagepub.com>

Scaling Hard Vertical Surfaces with Compliant Microspine Arrays

Alan T. Asbeck, Sangbae Kim, M. R. Cutkosky, William R. Provancher and Michele Lanzetta

The International Journal of Robotics Research 2006; 25; 1165

DOI: 10.1177/0278364906072511

The online version of this article can be found at:
<http://ijr.sagepub.com/cgi/content/abstract/25/12/1165>

Published by:

 SAGE Publications

<http://www.sagepublications.com>

On behalf of:



Multimedia Archives

Additional services and information for *The International Journal of Robotics Research* can be found at:

Email Alerts: <http://ijr.sagepub.com/cgi/alerts>

Subscriptions: <http://ijr.sagepub.com/subscriptions>

Reprints: <http://www.sagepub.com/journalsReprints.nav>

Permissions: <http://www.sagepub.com/journalsPermissions.nav>

Citations (this article cites 20 articles hosted on the
SAGE Journals Online and HighWire Press platforms):
<http://ijr.sagepub.com/cgi/content/abstract/25/12/1165#BIBL>

Alan T. Asbeck
Sangbae Kim
M.R. Cutkosky

School of Engineering
Stanford University
Stanford, California 94305-2232
{aasbeck,sangbae,cutkosky}@stanford.edu

William R. Provancher

Department of Mechanical Engineering
University of Utah
Salt Lake City, Utah 84112-9208
wil@mech.utah.edu

Michele Lanzetta

University of Pisa
Pisa, Italy
michele.lanzetta@ing.unipi.it

Scaling Hard Vertical Surfaces with Compliant Microspine Arrays

Abstract

A new approach for climbing hard vertical surfaces has been developed that allows a robot to scale concrete, stucco, brick and masonry walls without using suction or adhesives. The approach is inspired by the mechanisms observed in some climbing insects and spiders and involves arrays of microspines that catch on surface asperities. The arrays are located on the toes of the robot and consist of a tuned, multi-link compliant suspension. The fundamental issues of spine allometric scaling versus surface roughness are discussed and the interaction between spines and surfaces is modeled. The toe suspension properties needed to maximize the probability that each spine will find a useable surface irregularity and to distribute climbing loads among many spines are detailed. The principles are demonstrated with a new climbing robot, SpinybotII, that can scale a wide range of flat exterior walls, carry a payload equal to its own weight, and cling without consuming power. The paper also reports how toe parameters scale with robot mass and how spines have also been used successfully on the larger RiSE robot.

KEY WORDS—bio-inspired, legged locomotion, climbing, spines

This work is an extension of two papers presented at conferences (see Asbeck et al. (2005) and Kim et al. (2005)).

The International Journal of Robotics Research
Vol. 25, No. 12, December 2006, pp. 1165-1179
DOI: 10.1177/0278364906072511
©2006 SAGE Publications

Figures appear in color online: <http://ijr.sagepub.com>

1. Introduction

In recent years, there has been considerable progress in small, legged robots that can run rapidly and stably over rough terrain (Saranli et al. 2001; Cham et al. 2002; Quinn et al. 2003, Fukuoka et al. 2003). Climbing and maneuvering on vertical surfaces presents a more difficult challenge, one that robots are just beginning to address. Small robots that can climb a variety of hard and soft surfaces unobtrusively and cling for extended periods of time without high power consumption would be beneficial for applications such as surveillance or the inspection of hard-to-reach locations.

Previously developed climbing robots have generally employed suction (LaRosa et al. 2002; Tummala et al. 2002, Zhu et al. 2002), magnets (Balaguer et al. 2000; Xu and Ma 2002) or adhesives (Menzel and D'Aluisio 2000; Daltorio et al. 2005a, 2005b) to cling to smooth vertical surfaces such as windows and interior walls. None of these approaches is suitable for porous or dusty exterior surfaces such as brick, concrete, stucco or stone. Other climbing robots employ hand and foot holds in the manner of a human climber (Bevly et al. 2000; Bretl et al. 2003). A recent innovation employing a controlled vortex (Vortex 2003) to create negative aerodynamic lift and force the robot against a surface has been demonstrated on brick and concrete walls with considerable success. However, this approach consumes significant power (including when the robot is stationary), unavoidably generates noise and is more difficult to adapt to non-flat surfaces such as window ledges and corners.

When we look at animals that exhibit agility on vertical surfaces, we find a variety of methods employed (Cartmill 1985). Larger animals such as cats and raccoons have strong claws that can penetrate wood and bark surfaces. Tree frogs and many insects employ sticky pads (Emerson and Diehl 1980; Federle et al. 2002). Geckos and some spiders utilize large numbers of very fine hairs that achieve adhesion via *van der Waals* forces on almost any kind of surface (Autumn and Peattie 2002; Kesel et al. 2003; Arzt et al. 2003). Other insects, arthropods and reptiles employ small spines that catch on fine asperities (Dai et al. 2002). All of these approaches are worthy of examination for climbing robots. However, dry adhesives and spines are particularly attractive for hard, dusty, exterior surfaces.

Several researchers are currently working on creating synthetic versions of the setae found on geckos or the scopulae seen on spiders (Menon et al. 2004; Sitti and Fearing 2003; Geim et al. 2003). The early results are intriguing but current synthetic adhesives are not able to sustain the tensile loads needed at the forelimbs of a climbing robot. Moreover, they are fragile and lack the self-cleaning property that allows geckos to climb dusty walls.

In nature, spines are found on a variety of animals. Insects and arthropods that climb well on vertical surfaces often have legs equipped with large numbers of small, sharp spines. At a larger scale, geckos that frequent rock surfaces such as cliffs and caves have small claws on each toe in addition to their dry adhesive structures (Zani 2000). Unlike the larger claws of a cat, spines do not need to penetrate surfaces. Instead, they engage small surface asperities. Several studies in the biology literature have considered the problem of spine/surface interaction. Dai et al. (2002) present a planar model of spine/asperity contact and compute the maximum load per spine as a function of spine strength, relative size of the spine tip versus that of an asperity, and coefficient of friction. As expected, for rough surfaces the mechanical strengths of the spine and asperity become the limiting factors; for smoother surfaces friction is more important, and the ability to pull along the surface is much reduced.

In the following sections, we examine the issues involved with using spines to adhere to surfaces. First, in Section 2 we analyze how spines interact with surfaces. We address the following questions: Where can spines of a certain size perch on a given surface? How does the number of perching-spots vary with spine size? In Section 3 we examine the strength of the spine/asperity contacts. The analysis in Sections 2 and 3 lends insight into the design considerations of climbing with spines: In order to attach a robot of a given mass to a given surface, how small do the spines need to be and how many of those spines are needed?

In Section 4 we discuss foot and leg design considerations for making spines attach to surfaces. In Section 5 we present the design of a climbing robot, SpinybotII, that uses spines to climb to a variety of wall surfaces. In particular, we discuss the

features of SpinybotII that facilitate load sharing among many spines. Finally, in Section 6 we discuss how toe compliance parameters scale with robot mass and how spines have been adapted to the much heavier RiSE robot (Saunders et al. 2006).

2. Spine/Surface Modeling

Numerical simulations were performed to model the behavior of spines interacting with surfaces. In general, the simulations fitted 2-D spine cross-sections to 2-D surface profiles and determined the locations where the simulated spine could perch on the profile. This analysis gives insight into what size spines are needed to climb various surfaces and the properties of a surface that make it climbable. This is a geometric analysis, indicating trends in the number of asperities (perchable regions) per unit length of surface. Spine and surface strength are also important considerations and are addressed in Section 3 and Appendix II.

Two-dimensional profiles of several stone and sandpaper surfaces were obtained using a profilometer (Taylor Hobson Talysurf Series 2), with a conical stylus (15° cone angle) terminating in a spherical tip of radius $2\ \mu\text{m}$. Profiles of rougher concrete surfaces were measured using a laser micrometer (Omron Z4M-N30V), since the profilometer could not measure very rough surfaces. The measured profiles were 5 cm long. The profilometer had a vertical resolution $0.426\ \mu\text{m}$ and samples were taken every $1\ \mu\text{m}$; the laser micrometer had a spot size $64\ \mu\text{m}$, a vertical resolution of $0.977\ \mu\text{m}$, and samples were taken every $2.4\ \mu\text{m}$.

In analyzing these profiles we consider a typical spine as shown in the photograph in Figure 1. The spine is a gently curved beam with a circular cross section that tapers to a rounded tip of radius r_s . The spine is attached to a robot limb that drives it toward the surface and subsequently strokes it downward along the surface, hoping to engage an asperity. In the simulation, we model the spine tip as a circle of radius r_s approaching the surface at an angle θ_a .

In Figure 2, a diagram of our model, a circle of radius r_s has approached the surface in a direction indicated by the *approach vector*. The surface shown in the figure is an actual profile of a rough-cut granite surface.

We create a *spine swept volume* from the spine tip circle, bounded at the upper edge by the angle θ_a and at the lower edge by a ray perpendicular to the surface face. A *traced surface* is formed by moving the spine swept volume over the profile and recording the position of the center of the spine tip circle. We assume that the details of the spine, including a conical spine end and the spine curvature, fall within the swept volume. Thus, the spine swept volume accounts for the fact that an actual spine is not able to reach all parts of the surface (e.g. the bottoms of deep pits) if it moves towards the surface at an angle or if it is oriented at an angle as it slides over the surface.

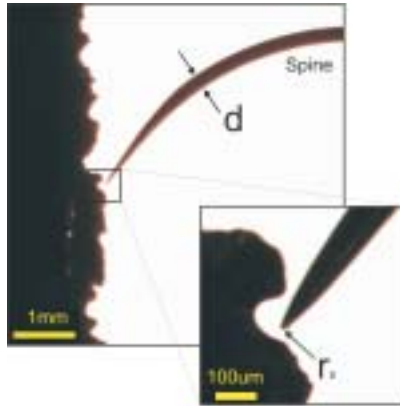


Fig. 1. Profile photograph of typical spine, with shaft dia., $d = 270\mu m$ and tip radius $r_s = 10\mu m$, engaging a profile of a rough concrete surface.

To find regions of the surface that a spine could perch on (i.e., asperities), we proceed along the traced surface from bottom to top in Figure 2. We search for locations in which the angle θ of the normal vector to the traced surface is above a minimum useable angle, θ_{min} , which depends on the angle at which the spines are loaded, θ_{load} , and coefficient of friction, μ , as seen in eq. (1):

$$\theta_{min} = \theta_{load} + \text{arccot}(\mu). \quad (1)$$

We consider regions between these locations and the subsequent minimum in the traced surface to be “useable asperities,” as shown in Figure 2. In essence, we find “shelves” that are terminated by an angle θ_{min} near regions of maximum projection from the wall surface. We assume that the spine slides quasi-statically along the surface from the top down. If the spine tip falls into any of the “useable asperity” regions, it will continue to move along the surface until it reaches the point at which the normal vector to the traced surface is at the angle θ_{min} , and at that location the spine will stop and catch on the surface. The spine can then be loaded away from the wall (i.e., used to generate adhesion) at an angle up to θ_{load} before it begins to slip off the asperity. For a given root-mean-square (RMS) surface roughness, R_q , the useable asperity regions can vary greatly, depending on the details of the profile. This purely geometric analysis does not account for spine bouncing or other dynamic effects; however, as discussed in the next section, it provides useful predictions of the comparative ease with which surfaces of varying roughness and asperity sharpness can be climbed.

We use the number of asperities per centimeter as a metric rather than other measures such as the effective length of the asperities because the former is a better indication of the probability that a spine will encounter an asperity during a stroke

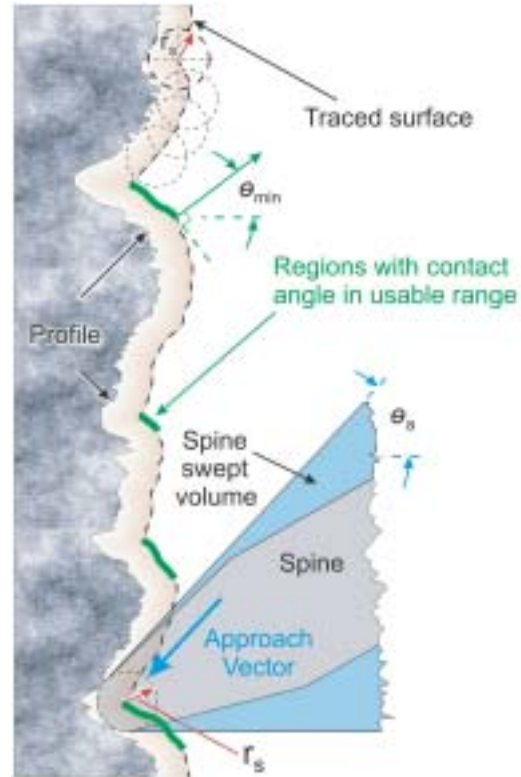


Fig. 2. Diagram of the spine/surface interaction model. The spine is modeled by a circle of radius r_s approaching in a direction indicated by the approach vector, which creates a swept volume. The intersection of the swept volume and the original profile is found and the center of the spine tip circle is recorded to create a traced surface. Contiguous shelf-like regions, starting when θ , the normal vector to the traced surface, is larger than some critical angle θ_{min} , are available for sustaining loads.

of a given length. (For example, a single long asperity would be equivalent to many short asperities in terms of effective asperity length.) A more accurate assessment would include complete information about the probability distribution of asperities and asperity lengths on the wall.

2.1. Simulation Results

Profiles were taken for several stone surfaces and several types of sandpaper, listed in Table 1. The table also shows the linear and RMS roughness measures R_a and R_q (see Appendix III) for these surfaces. Figure 3 shows typical results for the number of asperities per centimeter for selected stone and sandpaper surfaces, with constant values of θ_{min} and θ_a . For the stone surfaces (solid lines) the number of asperities per centimeter decreases at a rate close to $1/r$ for smaller tip radii. This is

Table 1. Table of Surfaces and Roughness Parameters

Surface Number	Surface	Average Roughness R_a (μm)	RMS Roughness R_q (μm)
1	cobblestone	56.9	78.1
2	machined granite	6.6	10.3
3	rough cut granite	42.7	56.1
4	polished granite	13.2	21.0
5	paving stone	73.0	92.2
6	concrete	93.0	131.9
7	cinderblock		
8	concrete 2	70.1	88.4
9	Al-oxide 80	42.1	57.0
10	Al-oxide 100	35.8	49.9
11	Al-oxide 120	20.3	26.0
12	Al-oxide 150	21.7	27.8
	Painter's 100	30.5	38.9

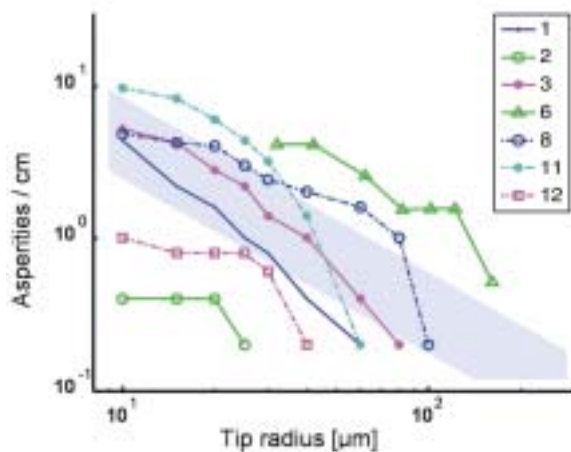


Fig. 3. Number of asperities per centimeter versus spine tip radius for various surfaces, with $\theta_a = 45^\circ$ and $\theta_{min} = 75^\circ$. The numbers in the legend correspond to the surfaces in Table 1. Solid lines indicate stone and concrete surfaces, and dashed lines indicate sandpaper surfaces. A band corresponding to the $1/r$ trend that would be expected for a perfect fractal surface has been added for reference. The surfaces not plotted had curves very similar to those shown.

to be expected, since many surfaces are approximately fractal (Costa and Cutkosky 2000; Greenwood 1992a, 1992b), so the surface properties should be similar at different length scales. Above a certain tip radius, however, the number of available asperities drops rapidly, implying that the surfaces do not behave fractally at large length scales. This is an effect of the

cutting, polishing and wearing processes that have partially smoothed the stone surfaces so that large asperities are rare.

The distribution of lengths between asperities is approximately described by an exponential random variable, with probability density function

$$f_x(x; \lambda) = \lambda \exp(-\lambda x), \quad x \geq 0, \quad (2)$$

where x is the distance between asperities and λ is the number of asperities per centimeter. The mean distance between asperities is $1/\lambda$ and the variance is $1/\lambda^2$. The asperity lengths are also approximately exponential random variables.

In Figure 3, the curves for the sandpaper surfaces have a shallow slope of less than $1/r$ for small tip radii. This occurs because the sandpaper surfaces have a relatively uniform particle size, so the number of asperities is closer to being a constant for small tip radii.

Figure 4 shows the number of asperities per centimeter versus spine tip radius for several values of θ_{min} and constant θ_a . As θ_{min} increases, corresponding to the need for asperities that are more shelf-like, the simulation is less likely to find useable asperities, as expected. This corresponds to a downward shift of the lines in the figure. All of the lines can be seen to follow the expected $1/r$ trend.

Figure 5 shows the number of asperities per centimeter versus θ_{min} and a constant spine tip radius. There are many asperities for low values of θ_{min} , which corresponds to regions of the surface that are nearly vertical. Making use of these asperities would require extremely high friction between the spines and surface as well as the spines being loaded nearly parallel to the surface. There are relatively few asperities for high values of θ_{min} , which correspond to shelf-like regions.

If θ_a is varied while holding θ_{min} constant, the number of asperities/cm changes relatively little, decreasing significantly only for large approach angles where the spine is nearly parallel to the wall. For small approach angles, the spine's ability to reach the regions of the surface it hooks on to is only slightly affected. In our analysis, we examined $\theta_a = 0^\circ, 45^\circ, 65^\circ$, and 80° . There was essentially no difference between any of the approach angles for 65° or less, while the 80° case showed a reduction in the number of asperities.

2.2. Correlation with Climbing Robot Performance

In this section we compare the results of the foregoing analysis to the empirical results obtained with our climbing robot. The parameters θ_{min} and θ_a used by our climbing robot, SpinybotII (see Figure 6), were measured and used in the simulation. Based on the geometry of SpinybotII, the feet are loaded at angles $3.5^\circ < \theta_{load} < 8^\circ$ degrees from the wall. The coefficient of friction between stainless steel spine tips and rock is generally between 0.15 and 0.25, which corresponds to θ_{min} between 86.5° and 81° for an average θ_{load} of 5° using Equation 1. The approach angle, θ_a , is from 45° – 65° , based on the angle of the spines themselves and the motion of the tip over

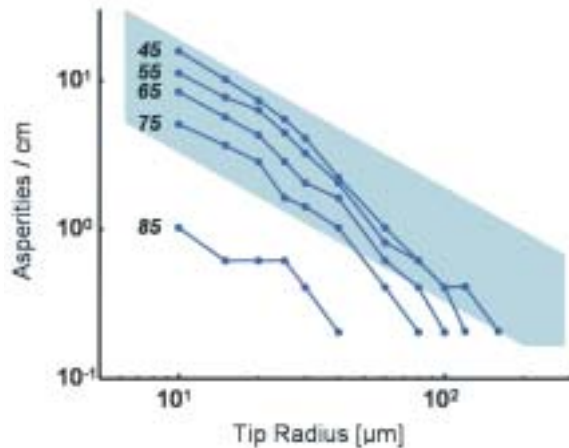


Fig. 4. Number of asperities per centimeter versus spine tip radius for several values of θ_{min} , for a stone surface (values of θ_{min} are marked on the graph). θ_a is held constant at 65° . A band corresponding to the $1/r$ curve expected for a perfect fractal surface is shown for comparison.

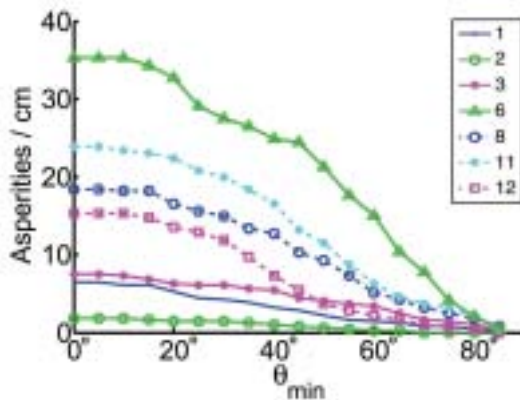


Fig. 5. Number of asperities per centimeter versus θ_{min} for various surfaces, for a constant spine tip radius of $30\mu\text{m}$. θ_a is held constant at 45° . The numbers in the legend correspond to the surfaces in Table 1. The number of asperities/cm can be seen to drop drastically as θ_{min} approaches 90° , showing that there are many fewer ledge-like regions that are perpendicular to the surface face than sloped regions more parallel to the surface face.

the surface. The tip radii, r_s , of the spines are $10\text{--}15\mu\text{m}$ for new spines and $25\text{--}35\mu\text{m}$ for spines dulled due to heavy use.

The results using these values qualitatively correspond to the actual performance of SpinybotII on the corresponding surfaces. SpinybotII can adhere extremely well to the Al-oxide 100 and 80 grit sandpapers, indicating that there is a high density of asperities with ledge angles of at least $81\text{--}86.5^\circ$.

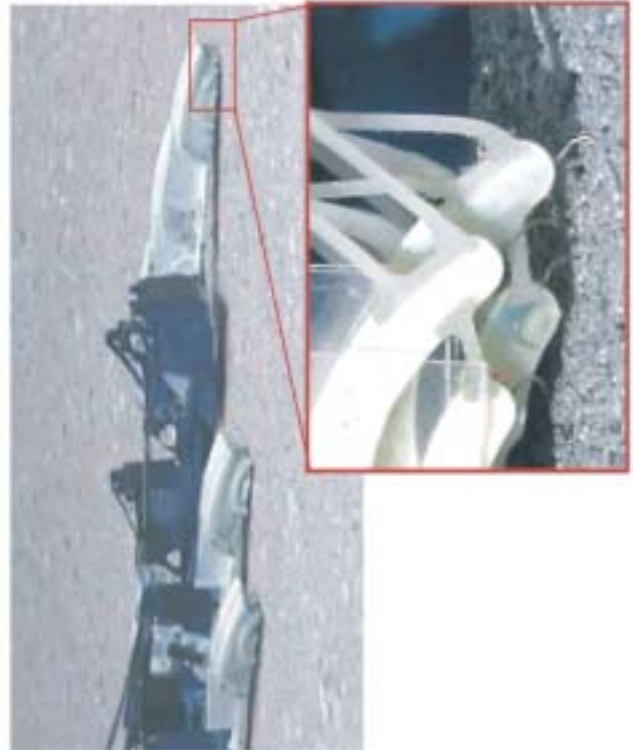


Fig. 6. Picture of upper section of SpinybotII on concrete wall and detailed view of several spines independently engaging asperities on the concrete surface.

SpinybotII adhere less well to the Al-oxide 150 and 120 grit sandpapers, with the feet slipping down these surfaces for a longer distance before solidly engaging, indicating a lower asperity density. It adheres poorly to the painter’s 100 grit sandpaper, only rarely finding asperities. On the natural surfaces, SpinybotII adheres very well to the rough concretes, moderately well (i.e., barely well enough to climb) to the rough cut granite surface, and not at all to the ground and polished surfaces. In the simulation, if θ_{min} is $82^\circ\text{--}85^\circ$ and θ_a is 45° or 65° , at radii of $10\text{--}40\mu\text{m}$ the ordering of the surfaces in terms of asperities/cm corresponds to the ordering of the same surfaces in terms of how well SpinybotII can adhere to them.

As discussed in the next section, SpinybotII’s spines do not scrape quasi-statically over surfaces. However, the effects of spine bouncing and reduced dynamic friction are mainly a reduction in the apparent asperity density. Also, asperity failure was not frequently observed for light loads on these surfaces. Thus, the relative ordering of how well SpinybotII’s feet perform on different surfaces generally matches the predicted ordering in terms of asperities per unit length in the simulation.

The concrete profiles show somewhat fewer asperities than would be expected for small tip radii and very large values of θ_{min} . This is because they were recorded using a laser micrometer with a 64 μm spot size that produced some low-pass filtering. Consequently the concrete profiles appear to have few asperities in the simulation using these parameters, although in actuality they have many asperities. Also, all of the surfaces show many fewer asperities than would be expected if θ_{min} is increased above around 82°. This discrepancy is likely due to the reduced ability of the measurement instruments to accurately record abrupt changes in surface height.

2.3. Discussion

Dai et al. (2002) present a planar model of spine/asperity contact that includes the relative size of the spine tip versus that of an asperity and coefficient of friction. Our analysis is similar, except that we use actual surface contours and compute the corresponding traced surface for the swept volume produced by a spine. Dai et al. state that the angle of spine/surface contact is key to obtaining traction between beetle claws and surfaces. However, they also discuss their results in terms of surface roughness, a different parameter entirely (though it is usually correlated with the spine/surface contact angles). Our analysis indicates that the normal angle, θ , is the critical parameter, and that the linear and RMS roughness measures R_a and R_q are not always correlated with actual spine performance. As an example, the R_a and R_q of the painter's 100 grit sandpaper are larger than the corresponding values for 120 and 150 grit Al-oxide, but it has many fewer useable asperities for large assumed values of θ_{min} , due to its more rounded features.

Our present analysis is limited in that it cannot detect the presence of angles more than 90 degrees (upward-leaning ledges). Even at angles close to 90 degrees it is less accurate due to the non-zero cone angle of the profilometer stylus. For some surfaces, SpinybotII's spines may attach to many asperities with angles greater than 90 degrees.

The observed behavior of spines interacting with surfaces also differs slightly from that assumed by the model. As a foot is brought into contact with a surface and begins its downward stroke, we observe that many spines briefly catch on "pseudo-asperities" and then break away as the load is ramped up. There are several reasons why the spines probably detach from these "pseudo-asperities." The spines can deflect slightly or undergo rotations, which will lead to their slipping. This can be due to non-idealities in the toe linkage design as well as spine bending. Another possibility is that these "pseudo-asperities" are actually valid asperities, but are quite weak and break off the wall once the load increases past a certain point (see Appendix II for analysis). Indeed, on some surfaces small particles can be observed breaking off the wall as a foot slides over it.

One final possibility is that the "pseudo-asperities" are regions where there is a ledge with a very shallow angle. In

these regions, initially a spine can get stuck if there is a small but positive normal force being applied to the spine and a small shear force. However, as the shear force is increased (and normal force possibly decreased), eventually the friction force between the spine and the ledge is not large enough to overcome the applied load, and the spine slips. These "pseudo-asperities" would be useable if the friction force between the spine and surface was higher or the loading angle was kept more towards the wall (or into the wall).

The spines also tend to skip over the surface (i.e., to become briefly airborne) after slipping off the "pseudo-asperities" and they undergo alternating regimes of static and dynamic friction. The effective coefficient of friction while this occurs is probably quite low. Finally, there is a chance that as a spine on a compliant suspension drags down the wall it may tend to follow a local groove or valley and thereby be steered away from protruding asperities. Conversely, negative asperities (pits) will tend to steer the spine into a favorable location for obtaining a grip. Hence, actual spine/surface dynamics vary depending on the surface type as well as how much the spine is able to move in the direction perpendicular to its travel.

It was mentioned earlier that the model does not take asperity strength into account. However, the trend of the number of asperities/cm varying as $1/r$ still should hold true, even if weak asperities are excluded. The strength of the asperities will depend on the material properties as well as surface geometry (see Appendix II).

3. Spine/Asperity Contact Strength

While smaller spines are more effective at engaging asperities on smooth surfaces, they also carry smaller loads. When steel spines catch on asperities, the contact typically fails in one of three ways:

- the spine fails plastically at its base due to tensile stress from bending,
- the spine tip rotates elastically such that it slips off the asperity,
- the asperity fails, typically as a particle becomes unbonded from the surrounding matrix.

In each of these cases, if we take a dimension such as the spine tip radius, r_s , as a characteristic length and scale everything uniformly, then the maximum load of the spine/asperity contact increases as r_s^2 (see Appendix II for details).

Figure 7 shows graphically how the maximum load of the spine/asperity contact increases as r^2 , while the expected number of asperities per unit area decreases as $1/r^2$. As spines become smaller we can ascend smoother surfaces because the density of useable spine/asperity contacts increases rapidly. However, to support a given load we need proportionally

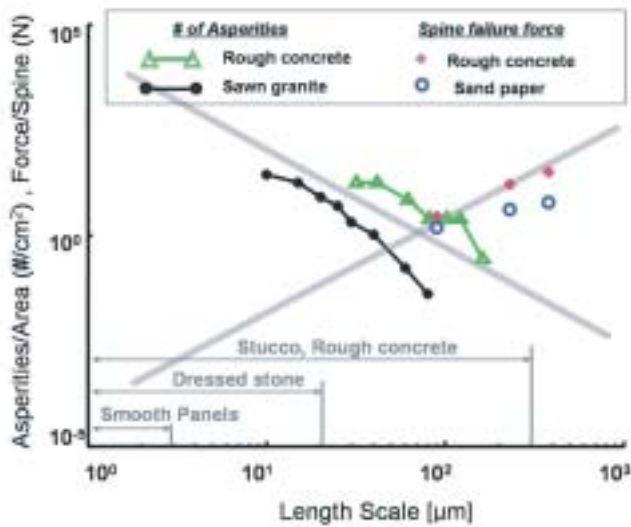


Fig. 7. Log/log plot showing the expected r^2 trend of spine/asperity contact strength versus the expected $1/r^2$ trend for asperities per unit area of the wall. The number of asperities per unit area for surfaces of rough cut granite and concrete are plotted for comparison with the expected asperity density trend. Individual tests of spine/asperity failures are plotted for concrete and sandpaper surfaces, showing the force required to break the spine/asperity contact. Failures occurred either through asperity brittle failure or spine bending (either elastically or plastically).

larger numbers of spines because each contact can sustain less force. Thus, in order to make use of large numbers of spines, the two key design principles are:

- ensure that as many spines as possible will independently attach to asperities,
- ensure the total load is distributed among the spines as uniformly as possible.

Figure 7 also shows data that supports the r^2 and $1/r^2$ trends for spine/asperity contact strength and asperity density per unit area, respectively. Measurements of contact strength were done using spines of various sizes on concrete and sandpaper samples attached to a load cell. We note that the sandpaper consisted primarily of male features (which had a small bonding cross-section). Therefore, asperity failure tended to occur before spine failure on that surface. In contrast, the cast concrete primarily consisted of female features that were much stronger; so spine failure, either by excessive end rotation or plastic bending, tended to dominate. For other surfaces, all three failure modes tended to occur simultaneously. The figure also shows the asperity density data for a concrete and

machined granite surface as compared to the expected $1/r^2$ for fractal surfaces. At the bottom of the figure, the representative asperity length scales for a few different surfaces are indicated. These indicate, for example, that rough concrete surfaces will present useable asperities of up to $300 \mu\text{m}$ in radius whereas smooth concrete or stone panels will present asperities of up to $20 \mu\text{m}$. These values essentially impose an upper limit to the spine size that can be used with these surfaces.

For our first climbing robot, SpinybotI, we employed four spines per foot, each with a tip radius of approximately $30\text{--}50 \mu\text{m}$. This machine was able to climb stucco and rough concrete reliably. The spine/asperity contacts could sustain loads of several newtons (N), usually limited by brittle failure of the asperity rather than of the spine. However, for surfaces such as smooth concrete and dressed stone, the probability of a spine encountering a useful asperity during a vertical stroke length of approximately 2 cm was too low for reliable climbing. SpinybotII employs two rows of spines on each foot, each spine having a tip radius of approximately $15\text{--}20 \mu\text{m}$. The maximum force per spine/asperity contact is $1\text{--}2 \text{ N}$, and the probability of finding useable asperities per centimeter of stroke length is high. On most surfaces that SpinybotII can climb, $30\text{--}40\%$ of the spines engage.

The design of feet that enable spines to effectively attach to asperities and share the load is described in Section 4. In addition, as with any climbing robot, it is important to keep the center of gravity as close to the wall as possible and to avoid imposing any forces or moments at the feet that could lead to premature detachment. The features of SpinybotII that achieve these effects are described in Section 5.

4. Toe and Foot Design: Promoting Attachment and Load Sharing

The feet on SpinybotII represent the sixth generation of a compliant, spined design. Each foot contains a set of ten identical planar mechanisms, or “toes,” as can be seen in Figure 8.

In discussing the toe and foot design, we assume that the foot undergoes a general motion to engage the spines on the wall. In particular, we assume the foot is presented to the wall in some orientation and is pressed against the wall lightly. The foot is then pulled downwards along the wall. In this manner, the spines undergo a motion similar to that assumed for an individual spine in the analysis in Section 2. The spines attach to the wall at some point while the foot is being dragged down the wall. The normal force must then decrease and eventually become negative for the spines to generate adhesion. During this process, the foot maintains its original orientation with respect to the wall.

Each of the toes is a compliant multi-bar linkage, independent of its neighbors and able to stretch parallel to the wall under a load. This feature of stretching along the wall under

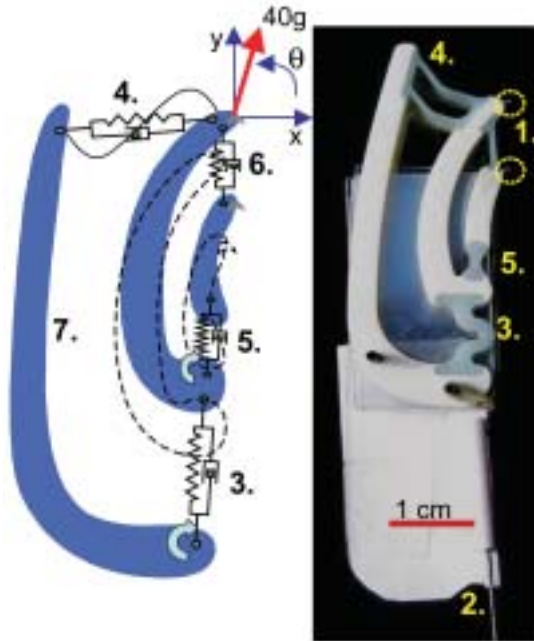


Fig. 8. Photograph and equivalent elastic linkages for one toe of SpinybotII. Linkage at left shows the deflected position for a 40 g load, superimposed on the undeflected position (shown in dotted lines). Key to labels: **1.** 200 μm shaft diameter spines (inside dotted circles), **2.** tendon for applying loads, **3.** soft urethane flexure permitting travel in y direction, **4.** buckling flexures with low stiffness in the $-x$ direction under compression and higher stiffness under tension, **5.** primarily rotational flexure for the proximal spine, **6.** buckling/lift-off flexure for proximal spine, **7.** hard member used to attach toe to tendon assembly.

a load is key to enabling multiple spines per foot to attach: if a toe catches an asperity, neighboring toes are not prevented from catching their own asperities because they will continue to slide down the wall as the caught toe stretches. Figure 6 shows a side view of the robot on a concrete wall and a detail of a single foot, showing several of the planar toe mechanisms, each of which bears two spines (several of which are visibly engaged). The manner in which the spines stretch along the wall independently can also be seen in Figure 9 in a top view of a foot.

The mechanisms are created using a rapid prototyping process, Shape Deposition Manufacturing (Merz et al. 1994; Binard and Cutkosky 2000) that permits hard and soft materials to be combined into a single structure. In the present case, the white and grey materials are hard and soft urethanes, of 75 Shore-D and 20 Shore-A hardness, respectively (Innovative Polymers Inc.). The resulting structure can be approximated as an elastic multi-link mechanism, as shown in Figure 8.

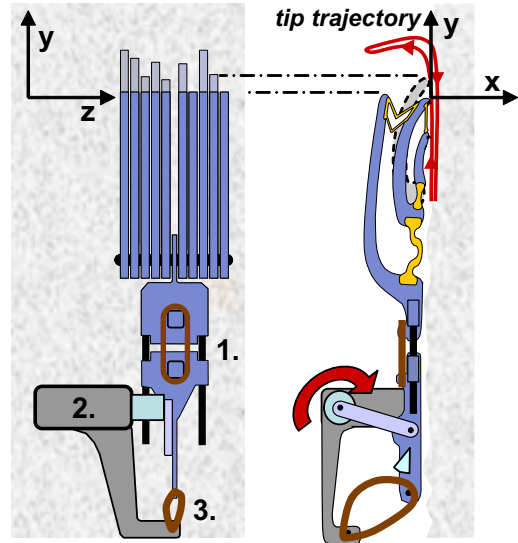


Fig. 9. Side and plan view of one foot containing ten toes. The toes can deflect independently of each other. In addition, the entire foot can displace in the distal (y) direction due to an un-actuated prismatic joint (**1**). The trajectory of the foot consists of detachment, an upward ($+y$) motion followed by a lift-off motion ($-x$), and attachment, consisting of touchdown ($+x$) and a downward pull ($-y$). The sequence of motions is accomplished using an under-actuated mechanism consisting of a single rotary RC servo motor (**2**) and an elastic band (**3**) that is taut while the foot is disengaged and becomes loose as the foot engages. See Figure 10 for further details about the foot actuation and trajectory.

The spines are approximately 1.5 mm long with a 200 μm shaft diameter and 10–35 μm tip radius. They are embedded directly into the hard white links during the SDM process. The soft urethane flexures provide both elasticity and viscoelastic damping. They permit greater extensions without failure than miniature steel springs (as were used on some of the earlier foot designs).

For small deflections, the linear and rotational stiffness of each spine in the (x, y) plane can be modeled using a 3x3 stiffness matrix, K , taken with respect to a coordinate system embedded in the spine (see Figure 8 for a diagram of the coordinate system):

$$\begin{bmatrix} k_{xx} & k_{xy} & k_{x\theta} \\ k_{xy} & k_{yy} & k_{y\theta} \\ k_{x\theta} & k_{y\theta} & k_{\theta\theta} \end{bmatrix}$$

For a spine to appropriately move along the wall and effectively engage asperities, this K matrix should have certain properties. At initial contact, k_{xx} should be very small for

displacements in the $-x$ direction, so that a large number of toes can conform to uneven surfaces without requiring a significant normal force. In SpinybotII's toes, this is accomplished through the flexures at the end of each toe (labeled 4. in Figure 8), which are designed to buckle so that they have a very low stiffness for $-x$ deflections. It is best to apply as small of a normal force as possible while engaging the spines because this will minimize the number of spines that attach to undesirable "pseudo-asperities", as discussed in Section 2.

If there are small tensile loads on the foot (in the $+x$ direction), some toes will remain compressed from the foot's engaging motions; k_{xx} should again be small so these compressed toes do not push the foot away from the wall. This concern presents a design compromise since a larger k_{xx} will bring the spines back to the wall more quickly if they should slip and bounce as described earlier. Finally, for moderate tensile loads such as are encountered when the foot is disengaging, k_{xx} should be large so the toes can disengage effectively. If k_{xx} is too small, spines can occasionally jam in deep pits on a surface as the foot moves away from the spine during disengagement. Jamming is prevented by pulling parallel to the spine axis with moderate tension. On SpinybotII this is also accomplished with the flexures at the end of the toe.

In the orthogonal direction, k_{yy} should be moderate, as it represents a different trade-off. A softer k_{yy} allows each toe to stretch more in the longitudinal direction to increase the probability that each spine will catch an asperity during the downward stroke of the foot; but if k_{yy} is too soft, the mechanism will require an excessive stroke length to support a given load. In essence, these factors determine the "asperity search length" for the downward stroke. At the same time, k_{xy} should be small so that stretching in the y direction does not cause the spines to retract. The $k_{x\theta}$ and $k_{y\theta}$ terms should also be small and, preferably, slightly negative so that displacements in the x or y direction are not accompanied by anticlockwise rotations in the (x, y) plane that would lead to premature disengagement.

The toes on SpinybotII were designed to conform to these requirements for effective spine attachment. Their actual behavior was confirmed by measurements. First, the stiffness matrix K was measured on a toe, for both the outer and inner spines, relative to the hard member of the toe that attached to the rest of the foot (7. in Figure 8). The stiffnesses were measured around an operation point of $(-0.13 \text{ cm}, 0.13 \text{ cm})$ in the (x, y) directions. The results are shown in Table 2, and they can be seen to generally correspond to the desired values as discussed previously.

The toe mechanism shown in Figure 8 was also modeled using Working Model™ software (MSC Inc.), and the various linear and rotational stiffness elements were adjusted to match bench-top test results of SpinybotII toes. The results are summarized in Table 3. The mechanism is designed so that initial contact at the inner, or proximal, spine actually forces

Table 2. SpinybotII Toe Stiffness Matrices

Outer Spine:			Inner Spine:		
16	-8	0.30	14	-2	0.25
-8	73	-0.28	-2	16	-0.01
0.30	-0.28	90	0.25	-0.01	58

Units:			K Matrix:		
N/m	N/m	N/rad	k_{xx}	k_{xy}	$k_{x\theta}$
N/m	N/m	N/rad	k_{xy}	k_{yy}	$k_{y\theta}$
N/rad	N/rad	N/rad	$k_{x\theta}$	$k_{y\theta}$	$k_{\theta\theta}$

Table 3. Stiffnesses and Damping Parameters for Toe Linkages

Location (numbered label, Fig. 8)	Parameter in kinematic model k = linear stiffness element c = linear damping element k_t = rotational stiffness element
3.	$k = 60 \text{ N/m}$ $c = 0.1 \text{ Ns/m}$ $k_t = 0.005 \text{ Nm}$
4.	$k = 90 \text{ N/m}$ in tension $k = 5 \text{ N/m}$ in compression $c = 0.02 \text{ Ns/m}$
5.	$k = 100 \text{ N/m}$ $c = 0.001 \text{ Ns/m}$ $k_t = 0.001 \text{ Nm}$
6.	$k = 60 \text{ N/m}$ $c = 0.1 \text{ Ns/m}$

the distal spine slightly outward ($+x$ direction) to increase the probability that it will also contact an asperity.

Once one or both spines have contacted the wall, the toe can apply a force that is mainly vertical, with a small inward ($+x$) component to help the robot climb. Figure 8 shows the effect of a typical 40 gram load sustained by one toe in climbing.

5. Body Design: Promoting Load Sharing and Stability

An important observation of agile scansorial animals like geckos is that they employ *multi-level conformability* (e.g. lamellae, toes, and limbs) and *redundancy* (multiple pads per toe, multiple toes per foot and multiple feet in contact) for reliable climbing. The same principles have been found necessary for SpinybotII. Accordingly, the entire foot mechanism is mounted on a prismatic joint with an elastic suspension that allows it to move up to 1 cm in the distal ($+y$) direction

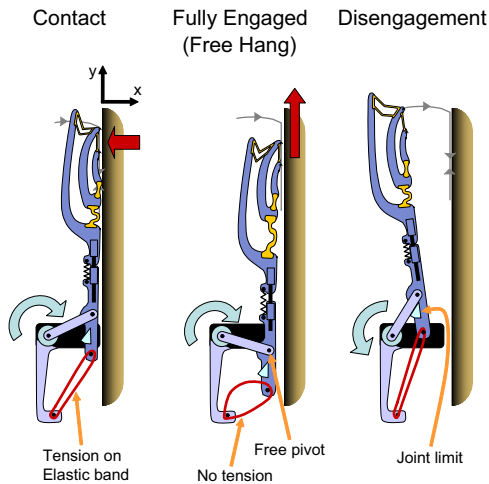


Fig. 10. Diagram of how the feet engage and disengage on SpinybotII. During engagement (left), the elastic band at the back of the leg unit is in tension. Since the foot is attached to the servo arm through a pin joint (labeled “free pivot” in the middle figure), the tension on the elastic band presses the foot against the wall as the servo rotates downward. The elastic band gradually loses its tension based on the geometry of the leg, such that when the foot is fully engaged there is no tension on the elastic band (middle). This allows the robot to hang freely from the foot and prevents forces that would push the robot body away from the wall. In disengagement (right), the servo reverses its direction of motion, reversing the trajectory of the foot. Eventually a hard stop on the foot hits the servo arm, causing the foot to lift off the wall.

(1. in Figure 9). In addition, the entire foot assembly is spring loaded by a second elastic element behind the pivot (3. in Figure 9), where it is connected to a rotary RC servo motor (2. in Figure 9). The result is an under-actuated R-R-P serial kinematic chain that traces a loop trajectory, as shown in Figure 9, when the servo motor rotates back and forth. Further explanation of the leg motion can be seen in Figure 10. After some experimentation, the best elastic elements were found to be 6.4 mm diameter elastic bands commonly used for dental braces.

This leg construction effectively moves the foot over the wall in a desirable manner similar to the “general motion” described earlier. The foot maintains its orientation parallel to the wall during the entire time it is touching the wall, and the positive normal force provided by the rear elastic element (3. in Figure 9) enables the spines to engage early in the stroke down the wall. The normal compliance of the foot provided by this elastic element also enables the foot to move over bumps or irregularities on the wall while maintaining contact.

When the leg has completed its downward motion, the elastic element goes slack, allowing the loading angle of the foot to be as close to the wall as possible, since the robot is then hanging freely from the foot by a pivot on the servo arm (see Figure 10).

The robot utilizes an alternating tripod gait, similar to that found in climbing insects (see Figure 11). At any time, the robot is nominally clinging by three feet. Like many climbing animals, the robot also has a tail which reduces the forces required at the front limbs to overcome body pitch-back from the wall. This pitch-back moment is produced by gravity acting at the center of mass, which is located approximately 2 cm outward from the wall. The weight of the robot, including lithium polymer batteries, wireless camera, and PIC microprocessor is 0.4 kg. It can carry an additional payload of 0.4 kg while climbing.

The climbing speed is currently quite slow (2.3 cm/s) but can easily be improved upon with the addition of structural damping in the limbs and toe suspension to prevent bouncing of the spines as they drag along the wall during the engagement stroke.

While the main concern for vertical climbing is to avoid pitching back from the plane of the wall, it is also important to maintain rotational stability in the plane of the wall so that momentary slips to not become catastrophic. As seen in Figure 11 the center of mass of SpinybotII lies within a polygon of contacts when three feet are attached to the wall. If only two feet are attached, the center of mass generally remains within the polygon, due to the elongated body design. Also, as observed in climbing insects and reptiles, the legs have a slight inward pull toward the centerline of the robot. This arrangement reduces the upsetting moments (in the plane of the wall) about the center of mass, should one of the legs momentarily lose its grip. If one of SpinybotII’s three attached feet loses its grip, the robot will continue, usually only suffering from a slight change in heading; if multiple feet lose their grip it falls.

SpinybotII is able to climb a wide range of flat vertical surfaces, including brick, stucco, concrete, rock, and other surfaces with similar roughness and fine-scale topology. A video of SpinybotII climbing various buildings around the Stanford campus and some close shots of its feet and toes engaging asperities can be seen in Extension 1. Watching the video closely will reveal several instances in which one foot briefly loses its grip. However, there is enough redundancy and compliance that the robot does not fall. Of course, if the robot encounters a very smooth patch, it either fails to proceed or falls. During several days of outdoor testing the robot rarely fell off the walls it was climbing. Most failures occurred at the end of the testing period and were probably due to the dulling of the spine tips that had taken place.

One problem encountered during testing was the tendency of toes to break occasionally due to overextension. Since the toes engage asperities probabilistically, sometimes one spine

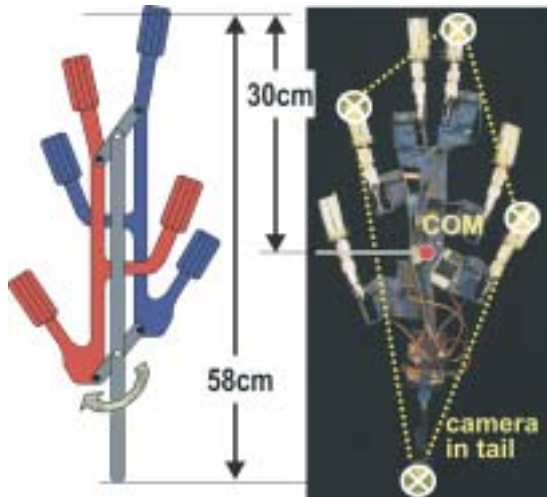


Fig. 11. Photograph of SpinybotII wall and diagram of climbing mechanism. Each set of three legs is attached to a mechanism that allows the robot to “ratchet” its way up the wall with an alternating tripod gait. A long tail helps to reduce the pitching moment. The center of mass (COM) is within the polygon of contacts, to minimize yawing rotations in the plane of the wall.

will attach to an asperity early in the foot’s engagement stroke while the other spines will not engage until much later. This puts a lot of force on the toe that attached early, occasionally exceeding the tensile strength of the extension flexure (3. in Figure 8) and causing it to break.

The other main problem that occurred during testing was the tendency of the robot to steer away from vertical while it was climbing. Since the robot was not controlled during its operation, asymmetries in foot attachment would lead to slight changes in heading that would accumulate over time. The robot was manually stopped if it deviated more than about 15° from vertical, but it usually had no trouble adhering to the wall even at these angles, due in part to the pull-in forces provided by the legs.

It was also noticed that the feet usually disengaged when the next tripod engaged, because the engagement motion moved the body slightly upwards. This was unintended but made disengagement smoother, as the feet did not need to scrape against the wall when the servos moved them through their disengagement trajectory.

6. Adapting Spines to other Robots

The design principles above can be readily applied to other robot platforms, with some adaptation required to accommodate larger loads. As discussed in the previous sections, the

Table 4. SpinybotII Specifications

Mass	0.4 kg
Max payload	0.4 kg
Climbing speed	2.3 cm/s
Distance: COM to wall surface	2.0 cm
Batteries	lithium polymer total 340 mAh, 7.4 V
Processor	40 MHz PIC
# Servo motors	7
Servo motor torque	0.37 Nm
Camera	0.02 kg

desired spine tip dimensions are primarily a function of the surfaces to be climbed, and not of robot size. Consequently, for a given spine size, a heavier robot requires more spines per foot and the risk of spine failure (or surface failure) is greater. In other words, it is more essential to load the spines uniformly. The loading problem is complicated by the need to tune the stiffnesses of the toes based on total robot weight and total number of spines, as discussed in Section 4. The toes also need to stretch independently of their neighbors to ensure that each spine has a high probability of engaging asperities and to ensure load sharing. Consequently, it does not suffice simply to make the toes robust and stiff.

The basic scaling relationships among the desired x - and y -stiffnesses, spine size, robot mass and number of spines are summarized in Table 5. The stiffness of the toes in the x -direction (k_{xx}) should vary as $1/n$, where n is the number of toes, in order to maintain constant stiffness over the entire foot. However, this stiffness should not depend on the mass of the robot m or the spine tip radius r_s . The stiffness of the toes in the y -direction (k_{yy}) should also vary as $1/n$, to maintain a constant stroke distance down the wall. This stiffness should also depend on the robot’s mass and spine tip radius. To maintain a constant stroke distance on the wall, it should vary as m since heavier loads will extend the toes more. It should also be inversely proportional to the spine tip radius r_s , because the distance required to find an asperity will usually vary as r_s . Usually the required number of toes n should be chosen based on the spine size, leading to $n \propto 1/r_s$ for a constant robot mass.

One situation that requires attention is if a robot climbs a surface with a low density of useable asperities, or a foot fails to attach properly to the wall. In these cases, very few spines will attach to the wall, causing them to have abnormally high loads. To prevent spine or toe damage, one possible solution is to employ overload stops for the toes such that the spines automatically disengage if the overload condition is reached.

Examples of toes that employ overload stops can be seen in Figure 12. These toes have been used on another robot, the RiSE platform, a 3.2 kg, 6-legged, 2-DOF/leg robot that

Table 5. Effect of Scaling Parameters on Desired Toe Stiffnesses

Stiffness (k_{ij})	X stiffness	Y stiffness
Number of toes n	$\propto 1/n$	$\propto 1/n$
Robot mass m	<i>constant</i>	$\propto m$
Spine tip radius r_s	<i>constant</i>	$\propto 1/r_s$



Fig. 12. Photograph of two toe designs that employ overload stops to prevent toe damage. A pin **1**, attached to the robot's foot provides overload protection in conjunction with the hole in each toe surrounding the pin. This ideally causes the toe to disengage upon excessive extension, or in the worst case prevents further extension if the toe does not disengage.

employs many of the same features as SpinybotII, including a tail, pull-in motions, and a sprawled posture with the center of mass close to the wall (Saunders et al. 2006). Although the RiSE platform is approximately 7.5 times heavier than SpinybotII, it has been able to climb multi-story stucco and rough concrete walls reliably due to its use of active force sensing (to avoid overloading any of the feet) and active steering to navigate around smooth patches. It presently cannot climb some of the surfaces SpinybotII can, but work is ongoing to equip it with smaller and more numerous spines.

7. Conclusions and Future Work

7.1. Conclusions

SpinybotII climbs reliably on a wide variety of hard, outdoor surfaces including concrete, stucco, brick, and dressed sandstone with average asperity radii $>25 \mu\text{m}$. The essential principles behind its operation include using many miniature spines with a compliant suspension that ensures that the load is shared uniformly among them. The same principles can also be applied to larger robot platforms. Desired spine tip radius is a function of average asperity size for the surfaces to be climbed and not of robot size.

A more challenging problem is to tackle rough or corru-

gated surfaces or, in general, surfaces that have roughness comparable to spine length. Either the feet and toes must have enough "suspension travel" to accommodate the contours of the surface or they must have an additional active degree of freedom, like the toes of geckos or the tendon-actuated tarsus of insect legs. On contoured surfaces it should be possible to exploit internal "grasp" forces, in a manner similar to that used by robots that climb with hand-holds and foot-holds (Bretl et al. 2003; Bevely et al. 2000), for additional security. The compliant suspension of the spines will become an increasingly difficult design challenge as spines are made smaller: smaller spines necessarily have a smaller clearance, possibly preventing them from reaching deep holes in the surface while maintaining a favorable loading angle.

Another challenging problem is to climb surfaces with much lower roughness than concrete or sandstone, such as polished stone or interior wall panels. The scaling arguments in Sections 2 and 3 should still apply. However, for smooth panels the average asperity radius may be on the order of a few micrometers, requiring spine tip radii of perhaps $1 \mu\text{m}$. These extremely small spines will be over 100 times weaker than the spines on SpinybotII and a large number of them will be required, unless the overall mass of the robot can be reduced correspondingly. Going still smaller, we approach the dimensions of the hairs that are being investigated for synthetic dry adhesives (Arzt et al. 2003; Menon et al. 2004; Sitti and Fearing 2003; Geim et al. 2003). At the smallest scales, hairs utilizing adhesion have two advantages over microspines or nanospines: they are less sensitive to the local surface normal distribution and they are loaded primarily in tension, rather than in bending.

For a given surface, at a small enough length scale, the surface will appear fractal. For spine dimensions smaller than this, the number of asperities per unit area will grow as $1/r^2$. Since the spine strength grows as r^2 , we hypothesize that the total weight that can be sustained per unit of surface area using spines is approximately constant. This weight per unit area number will depend on the distribution of surface normal angles, which is related to the surface's fractal dimension.

An interesting question is whether some combination of spines and adhesive hairs will ultimately prove most effective for scaling a variety of hard vertical surfaces. Different surfaces have different distributions of surface normal angles. Spines perform best on surfaces with normal angles close to 90° , while dry adhesives do best on smoother surfaces with normal angles closer to 0° . To be able to climb the widest variety of surfaces, both spines and dry adhesives could be used.

7.2. Future work

Future work in modeling spine/surface contacts could benefit from 3-D surface measurement, which would enable more accurate asperity location predictions. For very smooth sur-

faces, an atomic force microscope or similar instrument may be required to accurately measure the surface heights. For rough surfaces, using a laser interferometer with the surface tilted at an angle could permit measurement of surface normal angles in excess of 90° . The model could also be extended to include asperity strength. For the robot feet, making smaller spines and better suspension systems is the corresponding next step. It is still unknown what the minimum scale is for fabricating and using spines effectively.

For the SpinybotII robot body, obvious improvements are to increase the climbing speed and to provide additional articulation so that the robot can negotiate vertical/horizontal transitions such as window sills. These features are being presently added to the RiSE robot, which will enable it to have a wide range of behaviors. Adding degrees of freedom is straightforward, except that the center of mass must remain close to the wall and the additional degrees of freedom must not interfere with the compliant design principles of the toes, feet and legs as described in this paper.

Appendix A: Spine Failure Modes

We have observed that the spine/asperity contacts have three primary failure modes.

1. The spine fails plastically at its base due to tensile stress from bending.
2. The spine deflects elastically such that it slips off the asperity.
3. The asperity fails, typically as a particle becomes unbonded from the surrounding matrix.

Figure 13 shows a curved beam used in spine failure mode analysis. Shown in the figure are the following variables, which are used in the subsequent calculations:

R = Radius of curvature of the spine,
 d = diameter of cross section of spine,
 β = angle from the y -axis to the tip of the spine,
 α = angle the tip of the spine rotates (about the z -axis) in response to
 F = force exerted on tip of the spine.

The first mode of failure is due to the tensile stress at the base of the spine. For a long curved spine, the maximum stress is essentially the same as it would be for a straight cantilever beam (Shigley and Mischke 1996):

$$\sigma_{max} = \frac{Mc}{I} = \frac{32Fl d}{\pi d^4} \propto \frac{1}{d^2} \quad (\text{if } \frac{l}{d} = \text{const}).$$

where

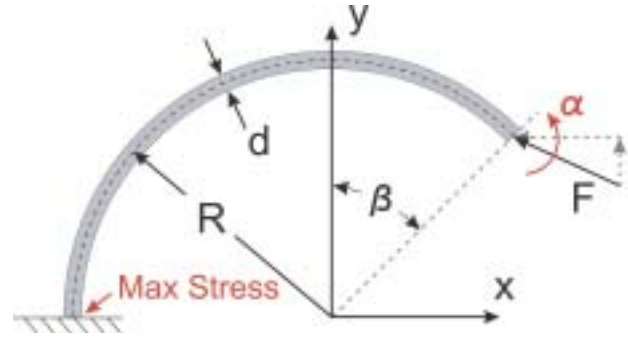


Fig. 13. Curved beam with variables used in spine failure mode analysis.

M = applied moment at end of beam

I = moment of inertia for circular beam cross-section

c = distance from the neutral axis of the beam to an edge

l = equivalent beam length.

The second mode of failure is excessive tip rotation. Here we can apply Castigliano's Theorem to solve for the tip deflections and rotations for a curved spine (Shigley and Mischke 1996). Applying a dummy end moment, M , and solving for the end rotation, α (see Figure 13), we obtain:

$$\begin{aligned} \alpha &= \partial U / \partial M \\ &= \frac{R^2}{2EI} [-2F_y + (2F_x + F_y(\pi + 2\beta))\cos(\beta) \\ &\quad + (-2F_y + F_x\pi + 2F_x\beta)\sin(\beta)] \propto \frac{1}{d^2} \\ &\quad (\text{if } \frac{R}{d} = \text{const. at given } \beta, F_x \text{ and } F_y) \end{aligned} \quad (3)$$

where

U = strain energy in the beam

E = Young's modulus for the beam material.

The third mode of failure is that the asperity itself may break off. The literature on surface failure or erosion (Momber 2004; Sheldon and Finnie 1966) for cementitious materials such as concrete, or rock with hard crystals in a weaker matrix, generally starts with the Hertz stress distribution at the contact (Johnson 1985). The maximum pressure is at the center of the contact patch:

$$p_{max} = 3f/2\pi a^2 = (6fE^2/\pi^3 R^2)^{1/3}$$

where

$$\begin{aligned} a &= (3fR/4E)^{1/3} \\ E &= (1 - \nu_s^2)/E_s + (1 - \nu_a^2)/E_a \\ (1/R &= 1/r_s + 1/r_a) \end{aligned}$$

and the subscripts s and a refer to the spine tip and asperity, respectively, and

ν = Poisson's ratio for each material

a = radius of the contact patch

f = normal force applied to the spine/asperity contact.

The variable r_s is the same variable discussed in Sections 2 and 3. This will be less than half of the beam diameter ($r_s < d/2$) in Figure 13 if a spine tapers to its point as shown in Figure 1.

The worst case tensile stress is at the periphery of the contact patch:

$$\sigma_T = ((1 - 2\nu_a)p_{max})/3$$

The actual failure will depend on the local stress state, number of cracks and fracture toughness of the material. However, it will be a function of the maximum tensile stress. Therefore we can write

$$f_{max} = [(\pi\sigma_{max}/(1 - 2\nu_a))^3(9/2E^2)]R^2$$

The quantity in square brackets is a constant depending on the materials so that, in the end, the maximum sustainable load is expected to vary as the square of the radii of curvature of the spine tip and asperity.

Appendix B: R_a and R_q Calculation

The linear roughness R_a was calculated by

$$R_a = \frac{1}{N} \sum_{i=1}^N abs(x[i] - \bar{x})$$

and RMS roughness R_q was calculated by

$$R_q = \sqrt{\frac{1}{N} \sum_{i=1}^N (x[i] - \bar{x})^2},$$

where $x[i]$ is the height of point i in the profile, \bar{x} is the average height of the profile, and N is the number of points in the profile.

Appendix C: Index to Multimedia Extensions

The multimedia extension page is found at <http://www.ijrr.org>.

Table of Multimedia Extensions

Extension	Type	Description
1	Video	A video of SpinybotII climbing various buildings around the Stanford campus and some close shots of its feet and toes engaging asperities.

Acknowledgment

This work was supported in part by the DARPA Biodynamics Program under Contract NC66001-03-C-8045. Additional support was provided by a DCI fellowship for W. Provancher and a NSF fellowship for A. Asbeck. The authors thank V. Mattoli for his development of the PIC processor program for controlling the RC servos. Thanks are also due to J. Lee for her help in designing and fabricating SpinybotI.

References

- Arzt, E., Gorb, S., and Spolenak, R. 2003. From micro to nano contacts in biological attachment devices. *Proceedings of National Academy of Sciences* 100:10603–10606.
- Asbeck, A. T., Kim, S., Provancher, W. R., Cutkosky, M. R., and Lanzetta, M. 2005. Scaling hard vertical surfaces with compliant microspine arrays. *Proceedings, Robotics: Science and Systems Conference*, Boston, MA, June.
- Autumn, K. and Peattie, A. 2002. Mechanisms of adhesion in geckos. *Integrative and Comparative Biology* 42(6):1081–1090.
- Balaguer, C., Gimenez, A., Pastor, J. M., Padron, V. M., and Abderrahim, C. 2000. A climbing autonomous robot for inspection applications in 3d complex environments. *Robotica* 18:287–297.
- Bevly, D., Dubowsky, S., and Mavroidis, C. 2000. A simplified cartesian-computed torque controller for highly geared systems and its application to an experimental climbing robot. *Transactions of the ASME. Journal of Dynamic Systems, Measurement and Control* 122(1):27–32.
- Binnard, M. and Cutkosky, M. R. 2000. A design by composition approach for layered manufacturing. *ASME Transactions, Journal of Mechanical Design* 122(1):91–101.
- Bretl, T., Rock, S., and Latombe, J. C. 2003. Motion planning for a three-limbed climbing robot in vertical natural terrain. *Proceedings of the IEEE International Conference on Robotics and Automation*, Piscataway, NJ, Vol. 205, pp. 2946–2953.
- Catmill, M. 1985. Climbing. In *Functional Vertebrate Morphology*, Eds M. Hildebrand, D.M. Bramble, K.F. Liem, and D.B. Wake), pp.73–88. The Belknap Press, Cambridge.
- Cham, J. G., Bailey, S. A., Clark, J. E., Full, R. J. and Cutkosky, M. R. 2002. Fast and robust: Hexapedal robots via shape deposition manufacturing. *The International Journal of Robotics Research* 21(10)pp???
- Costa, M. A. and Cutkosky, M. R. 2000. Roughness perception of haptically displayed fractal surfaces. *Proceedings of the ASME Dynamic Systems and Control Division* 69(2)1073–1079.
- Dai, Z. D., Gorb, S. N., and Schwarz, U. 2002. Roughness-dependent friction force of the tarsal claw system in the beetle *pachnoda marginata* (coleoptera, scarabaeidae). *Journal Of Experimental Biology* 205(16):2479–2488.

- Daltorio, K. A., Gorb, S., Peressadko, A., Horchler, A. D., Ritzmann, R. E., and Quinn, R. D. 2005a. A robot that climbs walls using micro-structured polymer feet. *International Conference on Climbing and Walking Robots (CLAWAR)*, p. 131–138.
- Daltorio, K. A., Horchler, A. D., Gorb, S., Ritzmann, R. E., and Quinn, R. D. 2005b. A small wall-walking robot with compliant, adhesive feet. *International Conference on Intelligent Robots and Systems (IROS)*, pp.4018–4023.
- Emerson, S. B. and Diehl, D. 1980. Toe pad morphology and mechanisms of sticking in frogs. *Biological Journal of the Linnean Society* 13(3):199–216.
- Federle, W., Riehle, M., Curtis, A. S. G., and Full, R. J. 2002. An integrative study of insect adhesion: mechanics and wet adhesion of pretarsal pads in ants. *Integrative and Comparative Biology* 42(6):1100–1106.
- Fukuoka, Y., Kimura, H., and Cohen, A. H. 2003. Adaptive dynamic walking of a quadruped robot on irregular terrain based on biological concepts. *International Journal of Robotics Research* 22(3-4):187–202.
- Geim, A. K., Dubonos, S. V., Grigorieva, I. V., Novoselov, K. S., Zhukov, A. A., and Yu, S. Shapoval. 2003. Microfabricated adhesive mimicking gecko foot-hair. *Nature Materials*, 2:461–463.
- Greenwood, J. A. 1992a. Contact of rough surfaces. In *Fundamental of Friction: Macroscopic and Microscopic Processes* (eds I. L. Singer and H. M. Pollock), pp.37–56. Kluwer Academic Publishers, Dordrecht.
- Greenwood, J. A. 1992b. Problem with surface roughness. In *Fundamental of Friction: Macroscopic and Microscopic Processes*, (eds I. L. Singer and H. M. Pollock), pp. 57–76. Kluwer Academic Publishers, Dordrecht.
- Johnson, K. L. 1985. *Contact Mechanics*, pp. 72–94. Cambridge University Press.
- Kesel, A. B., Martin, A., and Seidl, T. 2003. Adhesion measurements on the attachment devices of the jumping spider *evarcha arcuata*. *The Journal of Experimental Biology* 206:2733–2738.
- Kim, S., Asbeck, A. T., Cutkosky, M. R., and Provancher, W. R. 2005. Spinybot: Climbing hard walls with compliant microspines. *Proceedings of the IEEE International Conference on Robotics and Automation*, July, Seattle, WA, pp.601–606.
- La Rosa, G., Messina, M., Muscato, G., and Sinatra, R. 2002. A low-cost lightweight climbing robot for the inspection of vertical surfaces. *Mechatronics*, 12(1):71–96.
- Menon, C., Murphy, M. and Sitt, M.. 2004. Gecko inspired surface climbing robots. *Proceedings of the IEEE International Conference on Robotics and Biomimetics (ROBIO)*, 2004.
- Menzel, P. and D'Aluisio, F. 2000. Biobots. *Discover*, 21(9):86–87.
- Merz, R., Prinz, F. B., Ramaswami, K., Terk, M., and Weiss, L. 1994. Shape deposition manufacturing. *Proceedings of the Solid Freeform Fabrication Symposium*, Vol. 1-8, August.
- Momber, A. W. 2004. Damage to rocks and cementitious materials from solid impact. *Rock Mechanics and Rock Engineering*, 37(1):57–82.
- Quinn, R. D., Nelson, G. M., Bachmann, R. J., Kingsley, D. A., Offi, J. Allen, T. J. and Ritzmann, R. E. 2003. Parallel complementary strategies for implementing biological principles into mobile robots. *International Journal of Robotics Research*, 22(3):169–186.
- Saranli, U., Buehler, M., and Koditschek, D. E. 2001. Rhex: A simple and highly mobile hexapod robot. *International Journal of Robotics Research* 20:616–631.
- Saunders, A., Goldman, D. I., Full, R. J., and Buehler, M. 2006. The RiSE climbing robot: Body and leg design. *Proc. SPIE Int. Soc. Opt. Eng.*, 6230:623017, May.
- Sheldon, G. L. and Finnie, I. 1966. The mechanism of material removal in the erosive cutting of brittle materials. *ASME Journal of Engineering for Industry* 88B:393–400.
- Shigley, C. R. and Mischke, J. E. 1996. In *Standard Handbook of Machine Design (2nd ed)*. McGraw-Hill.
- Sitti, M. and Fearing, R. S. 2003. Synthetic gecko foot-hair micro/nano-structures for future wall-climbing robots. *Proceedings of the IEEE International Conference on Robotics and Automation*, Piscataway, NJ, Vol. 1, pp. 1164–1170.
- Tummala, R., Mukherjee, R., Xi, N., Aslam, D., Dulimarta, H., Xiao, Jizhong Minor, M., and Dang, G. 2002. Climbing the walls [robots]. *IEEE Robotics and Automation Magazine*, 9(4):10–19.
- Vortex HC, LLC. 2003. VRAM Mobile Robot Platform. [Online], <http://www.vortexhc.com/vmrp.html>.
- Xu, Z. L. and Ma, P. S. 2002. A wall-climbing robot for labelling scale of oil tank's volume. *Robotica*, 20:209–212.
- Zani, P. A. 2000. The comparative evolution of lizard claw and toe morphology and clinging performance. *Journal of Evolutionary Biology* 13:316–325.
- Zhu, J., Sun, D., and Tso, S. K. 2002. Development of a tracked climbing robot. *Journal Of Intelligent and Robotic Systems* 35(4):427–444.